PHYSICAL REVIEW D **89,** 084020 (2014)

Microlensed image centroid motions by an exotic lens object with negative convergence or negative mass

Takao Kitamura, Koji Izumi, Koki Nakajima, Chisaki Hagiwara, and Hideki Asada

Faculty of Science and Technology, Hirosaki University, Hirosaki 036-8561, Japan

(Received 25 July 2013; published 3 April 2014)

Gravitational lens models with negative convergence inspired by modified gravity theories, exotic matter, and energy have been recently examined in such a way that a static and spherically symmetric modified spacetime metric depends on the inverse distance to the nth power ($n = 1$ for Schwarzschild metric, $n = 2$ for Ellis wormhole, and $n \neq 1$ for an extended spherical distribution of matter such as an isothermal sphere) in the weak-field approximation. Some of the models act as if a convex lens, whereas the others are repulsive on light rays like a concave lens. The present paper considers microlensed image centroid motions by the exotic lens models. Numerical calculations show that, for large n cases in the convex-type models, the centroid shift from the source position might move on a multiply connected curve like a bow tie, while it is known to move on an ellipse for the $n = 1$ case and to move on an oval curve for $n = 2$. The distinctive feature of the microlensed image centroid may be used for searching (or constraining) localized exotic matter or energy with astrometric observations. It is shown also that the centroid shift trajectory for concave-type repulsive models might be elongated vertically to the source motion direction like a prolate spheroid, whereas that for convex-type models such as the Schwarzschild one is tangentially elongated like an oblate spheroid.

DOI: 10.1103/PhysRevD.89.084020 PACS numbers: 04.40.-b, 95.30.Sf, 98.62.Sb

I. INTRODUCTION

The bending of light is among the first experimental confirmations of the theory of general relativity. As one of the important tools in modern astronomy and cosmology, the gravitational lensing is widely used for investigating extrasolar planets, dark matter, and dark energy.

The light bending is also of theoretical importance, in particular for studying a null structure of a spacetime. A rigorous form of the bending angle plays an important role in understanding properly a strong gravitational field [1–6,8,9]. For example, strong gravitational lensing in a Schwarzschild black hole was considered by Frittelli, Kling, and Newman [1], by Virbhadra and Ellis [2], and more comprehensively by Virbhadra [3]; Virbhadra, Narasimha, and Chitre [4] studied distinctive lensing features of naked singularities. Virbhadra and Ellis [5] and Virbhadra and Keeton [6] later described the strong gravitational lensing by naked singularities; DeAndrea and Alexander [7] discussed the lensing by naked singularities to test the cosmic censorship hypothesis; Eiroa, Romero, and Torres [8] treated Reissner–Nordström black hole lensing; Perlick [9] discussed the lensing by a Barriola–Vilenkin monopole and also that by an Ellis wormhole.

One of peculiar features of general relativity is that the theory admits a nontrivial topology of a spacetime, for instance, a wormhole. An Ellis wormhole is a particular example of the Morris–Thorne traversable wormhole class [10–12]. Furthermore, wormholes are inevitably related with violations of some energy conditions in physics [13]. For instance, dark energy is introduced to explain the observed accelerated expansion of the Universe by means of an additional energy-momentum component on the right-hand side of the Einstein equation. Furthermore, the left-hand side of the Einstein equation, equivalently the Einstein– Hilbert action, could be modified in various ways (nonlinear curvature terms, higher dimensions, and so on) inspired by string theory, loop quantum gravity, and so on. Because of the nonlinear nature of gravity, modifications to one (or both) side(s) of the Einstein equation might admit spacetimes significantly different from the standard Schwarzschild spacetime metric, even if the spacetime is assumed to be asymptotically flat, static, and spherically symmetric. One example is an Ellis wormhole (being an example of traversable wormholes).

Many years ago, scattering problems in wormhole spacetimes were discussed (for instance, Refs. [14,15]). Interestingly, the Ellis wormhole has a zero mass at the spatial infinity, but it causes the light deflection [14,15]. Moreover, the gravitational lensing by wormholes has been recently investigated as an observational probe of such an exotic spacetime [9,16–23]. Several forms of the deflection angle by the Ellis wormhole have been recently derived and often used [9,18–21,24,25]. A reason for such differences has been clarified by several authors [26,27].

Small changes in gravitational lensing in modified gravity theories such as $f(R)$ and fourth-order gravity have been studied (e.g., Refs. [28–31]). Furthermore, Horvath, Gergely, and Hobill [32] studied lensing effects with negative convergence by so-called tidal charges in the Dadhich *et al.* solution, in which, for a braneworld black

hole, the tidal charge arises from tidal forces acting at the brane-bulk boundary [33]. A point is that negative convergence in this case does not require any exotic matter.

Inspired by a number of works on modifications in gravitational lensing, Kitamura *et al.* [34] assume, in a phenomenological sense, that an asymptotically flat, static, and spherically symmetric modified spacetime could depend on the inverse distance to the power of positive n in the weak-field approximation. The Schwarzschild spacetime and the Ellis wormhole correspond to $n = 1$ and $n = 2$, respectively, so that these spacetimes can be expressed as a one-parameter family. This one-parameter model expresses a spherical mass distribution. Note that Birkhoff's theorem could say that cases $n \neq 1$ might be nonvacuum, if the models were interpreted in the framework of the standard Einstein equation.

Kitamura *et al.* [34] have shown that demagnification could occur for $n > 1$ including the Ellis wormhole case ($n = 2$). They have also shown that time-symmetric demagnification parts might appear in light curves due to gravitational microlensing effects by such exotic models, where light curves are useful in microlensing observations in our Galaxy. For cosmological situations, however, the Einstein ring size becomes so large, and hence the typical time scale is so long that light curves cannot be observable in cosmology. On the other hand, the image separation angle becomes sufficiently large so that it can be practically measured. By using the latest result in the Sloan Digital Sky Survey Quasar Lens Search, Takahashi and Asada have recently set the first upper bound on the cosmic abundances of Ellis wormholes and also negative-mass compact objects [35]. In theoretical physics, negative mass is a hypothetical concept of matter for which the mass is of opposite sign to the mass of normal matter. Although possible negative mass ideas have been often discussed since the 19th century, there has been no evidence for them [36–39]. The negative masses might attract each other to form a negative massive clump so that such clumps could reside in cosmological voids (e.g., Ref. [40]). Gibbons and Kodama [41] have shown that curvature-regular asymptotically flat solitons with negative mass are contained in the Myers–Perry family, although the soliton solutions in the odd spacetime dimensions might not express real astrophysical objects.

However, the information on the image separation angle is not sufficient for distinguishing exotic lens models. Hence, Izumi *et al.* [42] have investigated gravitational lensing shear by an exotic lens object with negative convergence or negative mass. They have shown that images by the lens models for the gravitational pull (like a convex lens in optics) are tangentially elongated, whereas those by the repulsive ones (like a concave lens) are radially distorted. Their study [42] might concern the strong (or weak) lensing surveys at the extragalactic or cosmological distance.

Therefore, the main purpose of the present paper is to study microlensed image centroid motions by such exotic gravitational lens models. Here, we focus on the microlensing in our Galaxy. Studies of centroid displacements of lensed images have been often done for the Schwarzschild lens [43–50]. Virbhadra and Keeton [6] have investigated the centroid displacement for naked singularities by using the Janis–Newman–Winicour solution. Toki *et al.* [20] have studied the centroid motion by an Ellis wormhole. The main results of the present paper are as follows. (1) For certain exotic lens models, the centroid shift from the source position might move on a multiply connected curve like a *bow tie* for large n cases, while it is known to move on an ellipse for the $n = 1$ case [43,47] and to move on an oval curve for $n = 2$ [20]. (2) For concave-type repulsive lens models, the centroid displacement might move on a simply connected curve but might be elongated vertically to the source velocity, while it is tangentially elongated for the Schwarzschild case.

We take the units of $G = c = 1$ throughout this paper.

II. MODIFIED SPACETIME MODEL AND MODIFIED LENS EQUATION

This section briefly summarizes the basics of the exotic lens models [34,42].

A. Modified bending angle of light

Following Kitamura *et al.* [34], the present paper assumes that an asymptotically flat, static, and spherically symmetric modified spacetime could depend on the inverse distance to the power of positive n in the weak-field approximation. We consider the light propagation through a four-dimensional spacetime, although the whole spacetime may be higher dimensional. The four-dimensional spacetime metric is expressed as

$$ds^2 = -\left(1 - \frac{\varepsilon_1}{r^n}\right)dt^2 + \left(1 + \frac{\varepsilon_2}{r^n}\right)dr^2 + r^2(d\Theta^2 + \sin^2\Theta d\phi^2) + O(\varepsilon_1^2, \varepsilon_2^2, \varepsilon_1\varepsilon_2), \quad (1)$$

where r is the circumference radius and ε_1 and ε_2 are small bookkeeping parameters in iterative calculations. The weak-field approximation means $\varepsilon_1/r^n \ll 1$ and $\varepsilon_2/r^n \ll 1$. Namely, we study a far field from the lens object as $r \gg \varepsilon_1^{1/n}$ and $r \gg \varepsilon_2^{1/n}$. Note that Eq. (1) is not valid in the strong field near $r = 0$ (please see Ref. [51] for more detail). Here, ε_1 and ε_2 may be either positive or negative, respectively. Negative ε_1 and ε_2 for $n = 1$ correspond to a negative mass (in the linearized Schwarzschild metric).

Without loss of generality, we focus on the equatorial plane $\Theta = \pi/2$, since the spacetime is spherically symmetric. The deflection angle of light is obtained at the linear order as [34]

$$\alpha = \frac{\varepsilon}{b^n}\int_0^{\frac{\pi}{2}} \cos^n\psi d\psi + O(\varepsilon^2), \tag{2}$$

where the integral is positive definite, b denotes the impact parameter of the light ray, and we define $\varepsilon \equiv n\varepsilon_1 + \varepsilon_2$. By absorbing the positive integral into the parameter ε, we rewrite the linear-order deflection angle simply as $\alpha = \bar{\varepsilon}/b^n$, where the sign of $\bar{\varepsilon}$ is the same as that of ε. This deflection angle recovers the Schwarzschild ($n = 1$) and Ellis wormholes ($n = 2$) cases. For $\varepsilon > 0$, the deflection angle of light is always positive, which means that the corresponding spacetime model causes the gravitational pull on light rays. For $\varepsilon < 0$, on the other hand, it is inevitably negative, which implies the gravitational repulsion on light rays like a concave lens.

We mention an effective mass. A simple application of the standard lens theory [52] suggests that the deflection angle of light in the form of $\alpha = \bar{\varepsilon}/b^n$ corresponds to a convergence (scaled surface mass density) as

$$\kappa(b) = \frac{\bar{\varepsilon}(1-n)}{2}\frac{1}{b^{n+1}}, \tag{3}$$

which implies an extended spherical distribution of matter (or energy) for $n \neq 1$ and a singular source only for $n = 1$.

For the weak-field Schwarzschild case ($n = 1$), it follows that the convergence vanishes. For $\varepsilon > 0$ and $n > 1$, the effective surface mass density of the lens object is interpreted as negative in the framework of the standard lens theory [34]. This means that the matter (and energy) need to be exotic if $\varepsilon > 0$ and $n > 1$. Also when $\varepsilon < 0$ and $n < 1$, the convergence is negative, and hence the matter (and energy) need to be exotic. Interestingly, when $\varepsilon < 0$ and $n > 1$, the convergence is positive everywhere except for the central singularity, and hence exotic matter (and energy) is not required in the framework of the standard lens theory, in spite of the gravitational repulsion on light rays. Attraction ($\varepsilon > 0$) and repulsion ($\varepsilon < 0$) in the above two-parameter models do not have a one-to-one correspondence to positive convergence $\kappa > 0$ and a negative one $\kappa < 0$. This point is summarized in Table I [42].

B. Modified Einstein radius

Under the thin lens approximation, it is useful to consider the lens equation as [52]

TABLE I. The sign of the convergence κ. It is the same as that of $\varepsilon(1-n)$ according to Eq. (3).

$\kappa > 0$	$\varepsilon > 0$ & $n < 1$
	$\varepsilon < 0$ & $n > 1$
$\kappa = 0$	$n = 1$
$\kappa < 0$	$\varepsilon > 0$ & $n > 1$
	$\varepsilon < 0$ & $n < 1$

$$\beta = \frac{b}{D_L} - \frac{D_{LS}}{D_S}\alpha(b), \tag{4}$$

where β denotes the angular position of the source and D_L, D_S, and D_{LS} are the distances from the observer to the lens, from the observer to the source, and from the lens to the source, respectively. Note that there is the mathematical consistency of the use of the lens equation, Eq. (4), where the trigonometric functions are approximated by their leading terms. The present paper studies the leading term in the deflection angle so that Eq. (4) can be mathematically consistent. On the other hand, if one wishes to include the next (and higher order) for the bending angle, the third-order (or higher-order) terms in the expansion of the trigonometric functions have to be taken into account in the lens equation because of the mathematical consistency [2,5,9].

For $\varepsilon > 0$, there is always a positive root corresponding to the Einstein ring for $\beta = 0$. The Einstein ring radius is defined as [42]

$$\theta_E \equiv \left(\frac{\bar{\varepsilon}D_{LS}}{D_S D_L^n}\right)^{\frac{1}{n+1}}. \tag{5}$$

If $\varepsilon < 0$, on the other hand, Eq. (4) has no positive root for $\beta = 0$. This is because this case describes the repulsive force. For later convenience in normalizing the lens equation, we define the (tentative) Einstein ring radius for $\varepsilon < 0$ as

$$\theta_E \equiv \left(\frac{|\bar{\varepsilon}|D_{LS}}{D_S D_L^n}\right)^{\frac{1}{n+1}}, \tag{6}$$

although the Einstein ring does not appear for this case. This radius gives a typical angular size for $\varepsilon < 0$ lenses.

Like Schwarzschild lenses, there might exist a photon sphere for $\varepsilon > 0$. The radius of the photon sphere for the spacetime metric by Eq. (1) might become

$$R_{\rm ps} = \left(\frac{(n+2)\varepsilon_1}{2}\right)^{1/n}. \tag{7}$$

See Ref. [53] for a more thorough discussion on the photon surfaces.

C. Modified lens equation: $\varepsilon > 0$ case

Following Izumi *et al.* [42], let us begin with the $\varepsilon > 0$ case. As already stated, the matter (and energy) needs to be exotic if $n > 1$. In the units of the Einstein ring radius, Eq. (4) is rewritten in the vectorial form as

$$\hat{\boldsymbol{\beta}} = \hat{\boldsymbol{\theta}} - \frac{\hat{\boldsymbol{\theta}}}{\hat{\theta}^{n+1}} \quad (\hat{\theta} > 0), \tag{8}$$

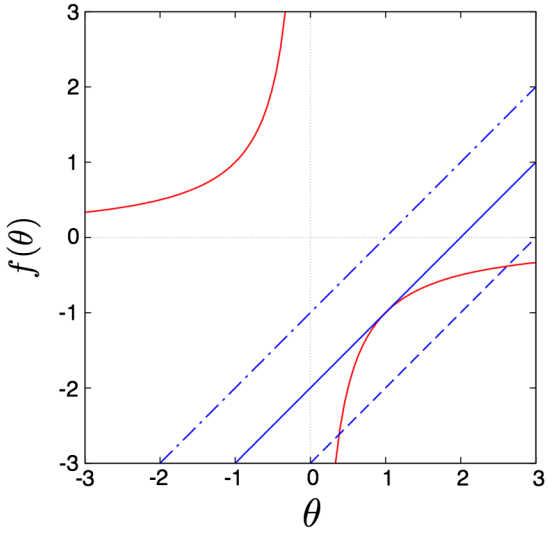

FIG. 1 (color online). Repulsive lens model ($\varepsilon < 0$). Solid curves denote $1/\hat{\theta}^n$, and straight lines mean $\hat{\theta} - \hat{\beta}$. Their intersections correspond to image positions that are roots for the lens equation. There are three cases: no image for a small $\hat{\beta}$ (dotted-dashed line), a single image for a particular $\hat{\beta}$ (dotted line), and two images for a large $\hat{\beta}$ (dashed line). The two images are on the same side of the lens object.

$$\hat{\boldsymbol{\beta}} = \hat{\boldsymbol{\theta}} - \frac{\hat{\boldsymbol{\theta}}}{(-\hat{\theta})^{n+1}} \quad (\hat{\theta} < 0), \tag{9}$$

where we normalize $\hat{\beta} \equiv \beta/\theta_E$ and $\hat{\theta} \equiv \theta/\theta_E$ for the angular position of the image $\theta \equiv b/D_L$, and $\hat{\boldsymbol{\beta}}$ and $\hat{\boldsymbol{\theta}}$ denote the corresponding vectors. There is always one image for $\hat{\theta} > 0$, while the other image appears for $\hat{\theta} < 0$ [34].

D. Modified lens equation: $\varepsilon < 0$ case

Next, let us mention the $\varepsilon < 0$ case [42]. In the units of the Einstein ring radius, Eq. (4) is rewritten in the vectorial form as

$$\hat{\boldsymbol{\beta}} = \hat{\boldsymbol{\theta}} + \frac{\hat{\boldsymbol{\theta}}}{\hat{\theta}^{n+1}} \quad (\hat{\theta} > 0), \tag{10}$$

$$\hat{\boldsymbol{\beta}} = \hat{\boldsymbol{\theta}} + \frac{\hat{\boldsymbol{\theta}}}{(-\hat{\theta})^{n+1}} \quad (\hat{\theta} < 0). \tag{11}$$

Without loss of generality, we assume $\hat{\beta} > 0$. Then, Eq. (11) has no root satisfying $\hat{\theta} < 0$, while Eq. (10) has

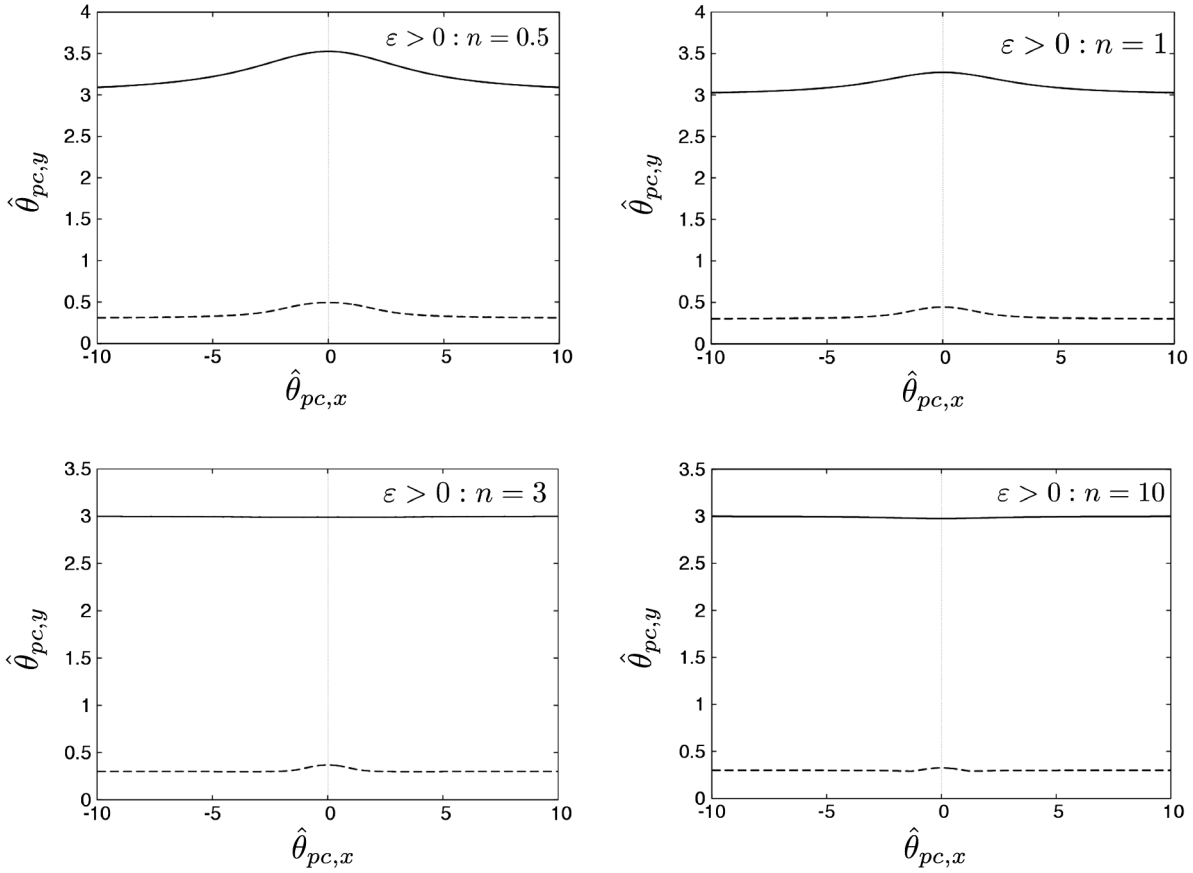

FIG. 2. Centroid motions as $(\hat{\theta}_{\mathrm{pc},x}, \hat{\theta}_{\mathrm{pc},y})$ for $\varepsilon > 0$ (convex-type attractive models). The solid and dashed curves correspond to $\hat{\beta}_0 = 3$ and $\hat{\beta}_0 = 0.3$, respectively. The horizontal axis along the source linear motion is $\hat{\theta}_{\mathrm{pc},x}$, and the vertical axis is $\hat{\theta}_{\mathrm{pc},y}$. Top left: $n = 0.5$ Top right: $n = 1$. Bottom left: $n = 3$. Bottom right: $n = 10$.

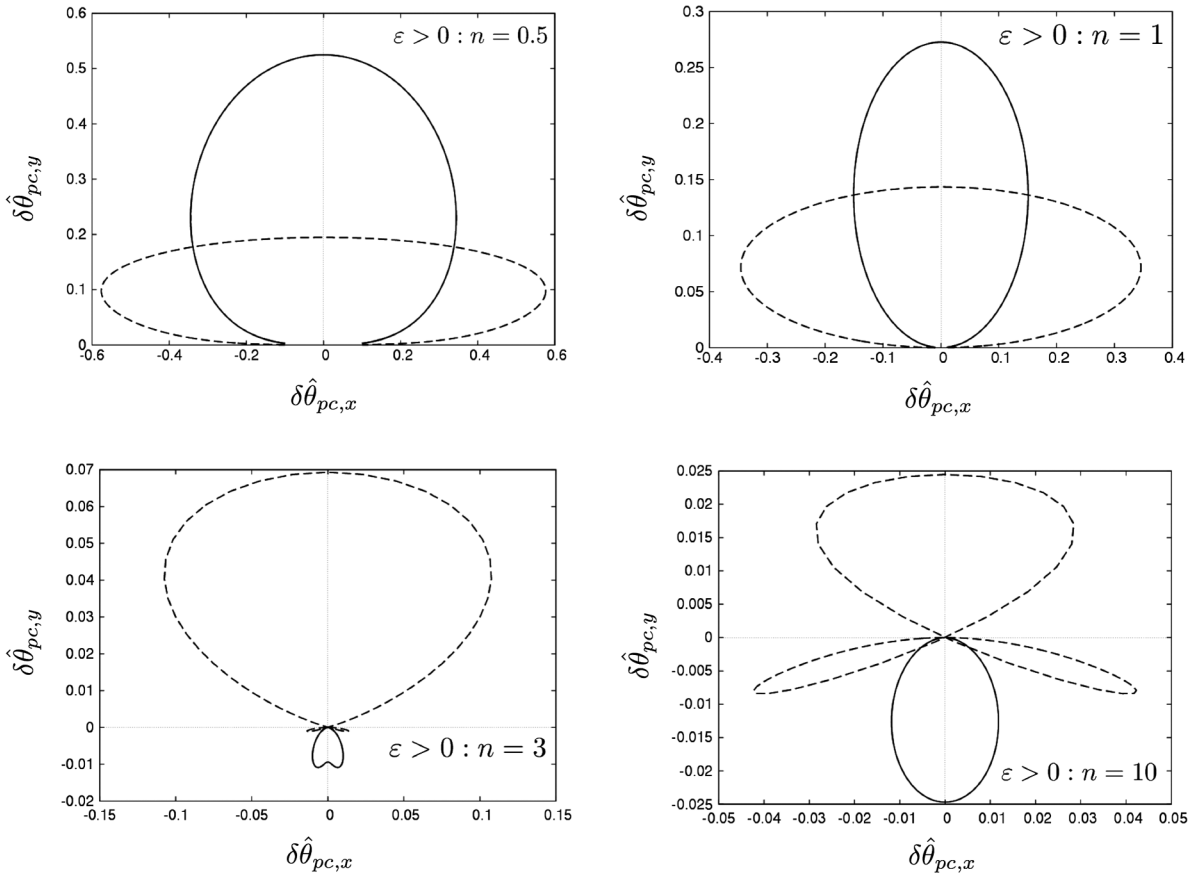

FIG. 3. Centroid shifts $\delta\hat{\theta}_{\rm pc}$ for $\varepsilon > 0$ (convex-type attractive models). The solid and dashed curves correspond to $\hat{\beta}_0 = 3$ and $\hat{\beta}_0 = 0.3$, respectively. The horizontal axis along the source velocity is $\delta\hat{\theta}_{{\rm pc},x}$, and the vertical axis is $\delta\hat{\theta}_{{\rm pc},y}$. Top left: $n = 0.5$ Top right: $n = 1$. Bottom left: $n = 3$. Bottom right: $n = 10$.

at most two positive roots. Figure 1 shows that there are three cases of the image number. For a large impact parameter case, two images appear on the same side with respect to the lens position, while no image appears for a small impact parameter. The only one image appears only when the impact parameter takes a critical value. Let us focus on the two image cases, from which the single image case can be discussed in the limit as the impact parameter approaches the particular value.

III. MICROLENSED IMAGE CENTROID

A. Image centroid

Let us study the microlensed image centroid motions. In any case of $\varepsilon > 0$ and $\varepsilon < 0$, the image positions are denoted by $\hat{\boldsymbol{\theta}}_1$ and $\hat{\boldsymbol{\theta}}_2$, and the corresponding amplification factors are denoted by A_1 and A_2. Without loss of generality, we take $\hat{\theta}_1 > \hat{\theta}_2$. In analogy with the center of the mass distribution, the centroid position of the light distribution of a gravitationally microlensed source is given by

$$\hat{\boldsymbol{\theta}}_{\rm pc} = \frac{A_1\hat{\boldsymbol{\theta}}_1 + A_2\hat{\boldsymbol{\theta}}_2}{A_{\rm tot}}, \tag{12}$$

where $A_{\rm tot}$ denotes the total amplification as $A_1 + A_2$. The corresponding scalar is defined as $\hat{\theta}_{\rm pc} \equiv (A_1\hat{\theta}_1 + A_2\hat{\theta}_2)A_{\rm tot}^{-1}$. Note that $\hat{\theta}_{\rm pc}$ is positive, when the centroid is located on the same side of the source with respect to the lens center.

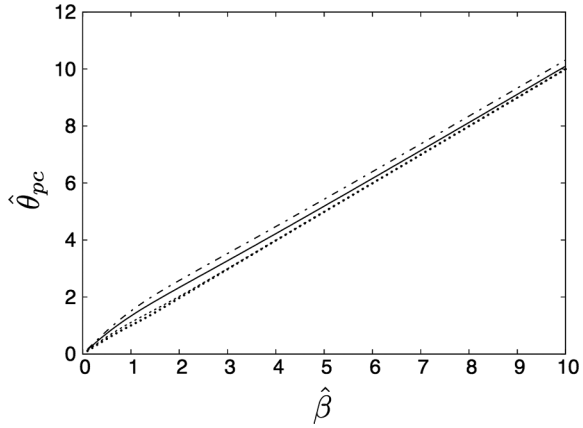

FIG. 4. Image centroid $\hat{\theta}_{\rm pc}$ and $\hat{\beta}$ for $\varepsilon > 0$ (convex-type attractive models). The dotted-dashed, solid, dashed, and dotted curves denote $n = 0.5$, 1, 3, and 10, respectively. The horizontal axis denotes the source position $\hat{\beta}$ normalized by the Einstein radius, and the vertical axis denotes $\hat{\theta}_{\rm pc}$.

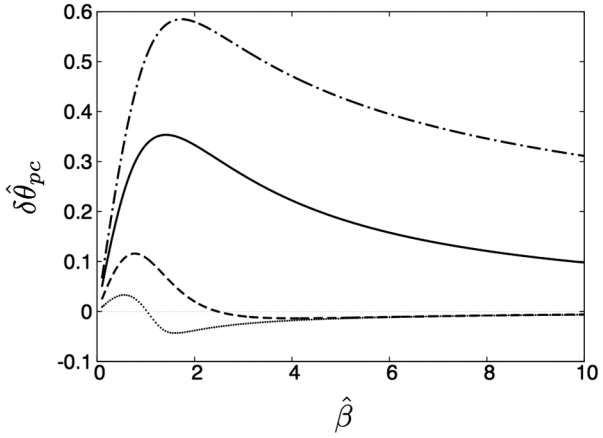

FIG. 5. Image centroid shift $\delta\hat{\theta}_{\rm pc}$ and $\hat{\beta}$ for $\varepsilon > 0$ (convex-type attractive models). The dotted-dashed, solid, dashed, and dotted curves denote $n = 0.5$, 1, 3, and 10, respectively. The horizontal axis denotes the source position $\hat{\beta}$ normalized by the Einstein radius, and the vertical axis denotes $\delta\hat{\theta}_{\rm pc}$.

The relative displacement of the image centroid with respect to the source position is written as

$$\delta\hat{\boldsymbol{\theta}}_{\rm pc} = \hat{\boldsymbol{\theta}}_{\rm pc} - \hat{\boldsymbol{\beta}}. \tag{13}$$

Henceforth, this is referred to as the centroid shift. The corresponding scalar is defined as $\delta\hat{\theta}_{\rm pc} \equiv \hat{\theta}_{\rm pc} - \hat{\beta}$. $\delta\hat{\theta}_{\rm pc}$ is positive when $\hat{\theta}_{\rm pc}$ is larger than $\hat{\beta}$.

By taking account of the relation between the lens and source trajectory in the sky, the time dependence of $\hat{\beta}$ is written as

$$\hat{\beta}(t) = \sqrt{\hat{\beta}_0^2 + (t - t_0)^2/{t_E}^2}, \tag{14}$$

where $\hat{\beta}_0$ is the impact parameter of the source trajectory and t_0 is the time of closest approach. Here, the source is assumed to be in uniform linear motion. We choose $t_0 = 0$. t_E is the Einstein radius crossing time given by

$$t_E = R_E/v_T, \tag{15}$$

where v_T is the transverse velocity of the lens relative to the source and observer. In the following numerical computations, time is normalized by the Einstein ring radius crossing time.

In making numerical figures, we employ $x - y$ coordinates, such that the coordinate origin is chosen as the lens center, the x axis is taken along the direction of the source

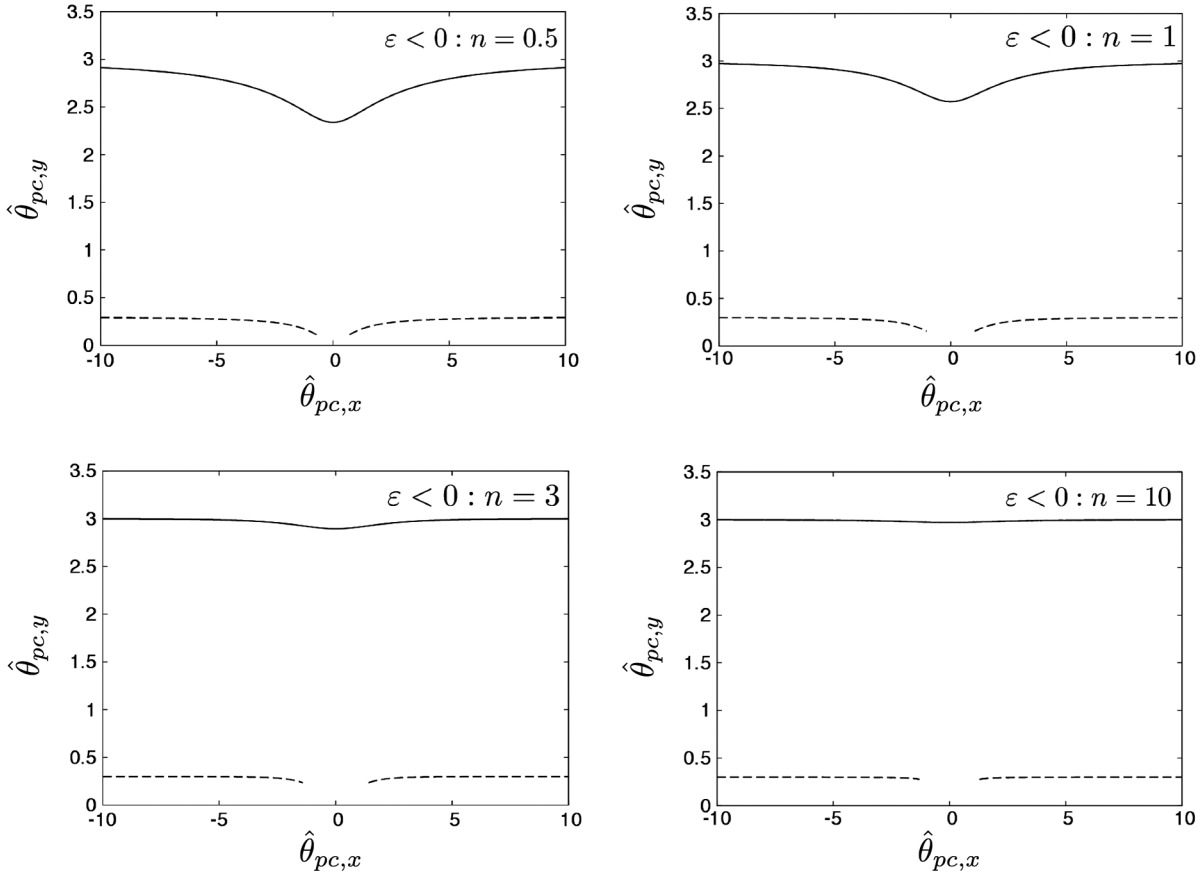

FIG. 6. Centroid motions as $(\hat{\theta}_{{\rm pc},x}, \hat{\theta}_{{\rm pc},y})$ for $\varepsilon < 0$ (repulsive models). The solid and dashed curves correspond to $\hat{\beta}_0 = 3$ and $\hat{\beta}_0 = 0.3$, respectively. The horizontal axis along the source linear motion is $\hat{\theta}_{{\rm pc},x}$, and the vertical axis is $\hat{\theta}_{{\rm pc},y}$. The dashed curves do not exist for small $\hat{\beta}$, where no images appear. Top left: $n = 0.5$ Top right: $n = 1$. Bottom left: $n = 3$. Bottom right: $n = 10$.

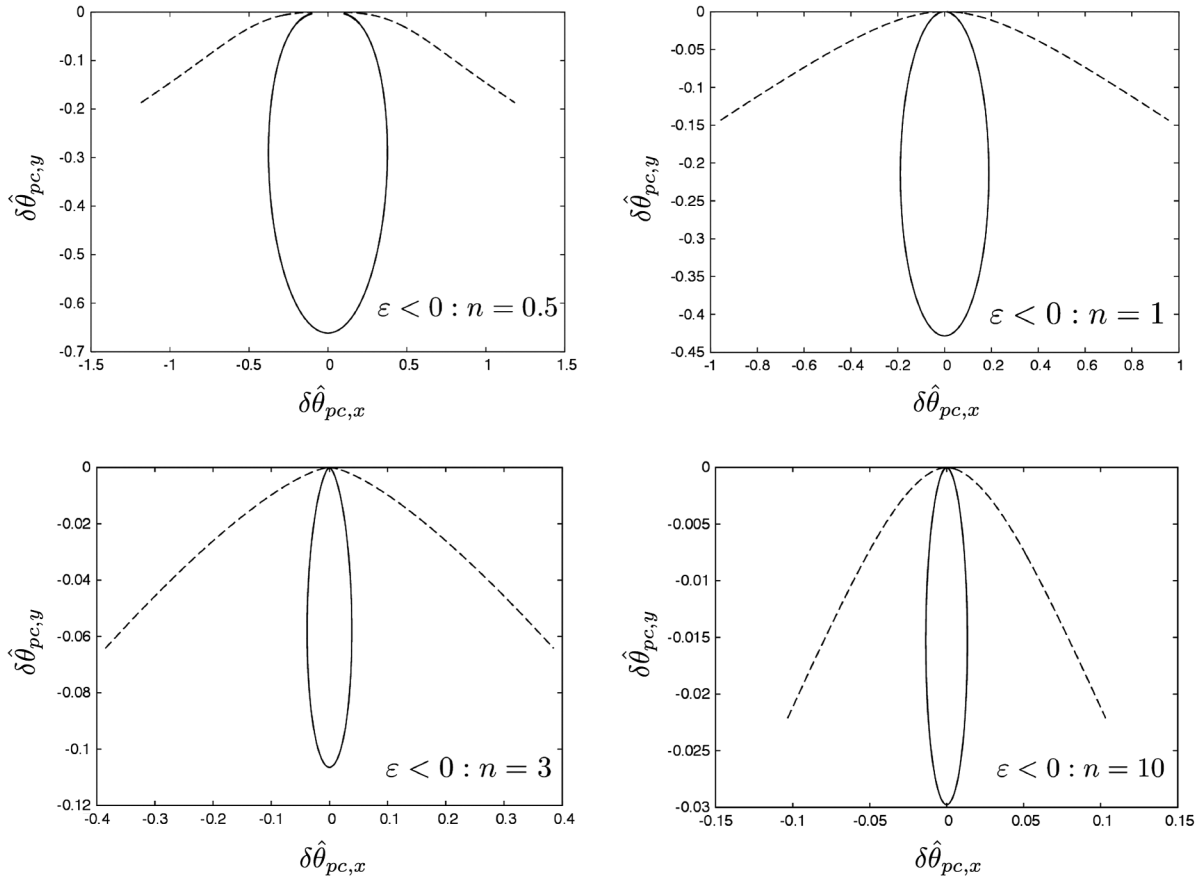

FIG. 7. Centroid shifts $\delta\hat{\boldsymbol{\theta}}_{\rm pc}$ for $\varepsilon < 0$ (concave-type repulsive models). The solid and dashed curves correspond to $\hat{\beta}_0 = 3$ and $\hat{\beta}_0 = 0.3$, respectively. The horizontal axis along the source velocity is $\delta\hat{\theta}_{{\rm pc},x}$, and the vertical axis is $\delta\hat{\theta}_{{\rm pc},y}$. The dashed curves are not closed because no images appear for small $\hat{\beta}$. Top left: $n = 0.5$ Top right: $n = 1$. Bottom left: $n = 3$. Bottom right: $n = 10$.

motion, and the y axis is perpendicular to the source motion.

B. Numerical computations: $\varepsilon > 0$ case

Let us begin with the $\varepsilon > 0$ case. See Fig. 2 for the image centroid trajectories by $\varepsilon > 0$ models for $\hat{\beta}_0 = 0.3$ and 3. Figure 3 shows the image centroid shift by the $\varepsilon > 0$ models. For $\hat{\beta}_0 = 0.3$, for instance, the maximum vertical shift of the image centroid position by the exotic lens models is $0.2(n = 0.5)$, $0.14(n = 1)$, $0.07(n = 3)$, and $0.02(n = 10)$ in the units of the Einstein ring radius, respectively. For $\hat{\beta}_0 = 3$, it is nearly $0.5(n = 0.5)$, $0.3(n = 1)$, $-0.01(n = 3)$, and $-0.02(n = 10)$. These results suggest that the astrometric lensing by the exotic models with large n is relatively weak compared with that by the Schwarzschild one ($n = 1$). In the weak-field region, one can understand the suppression of the anomalous shift of the image centroid position for large n because the bending angle by the large n models is proportional to the inverse impact parameter to the power of n, whereas that by the Schwarzschild lens depends on the inverse impact parameter.

A distinctive feature is that in $\varepsilon > 0$ and $n > 2$ cases bow knots might be added into the centroid shift trajectory, while the trajectory is known to be an ellipse for the $n = 1$ case [43,47] and to be oval for $n = 2$ [20]. Such a multiply connected shape of the centroid shift orbit would be an evidence of the corresponding exotic lens in astrometric observations. Figure 3 shows the bow-tie shape might disappear when the impact parameter becomes sufficiently large, for instance $\hat{\beta} \sim 3$. For $\varepsilon > 0$ and $n = 3$, the centroid shift could be negative for the $\hat{\beta}_0 = 3$ case. This is partly because A_2 becomes large compared with the $n = 1$ case.

At the center of the bow tie in the centroid shift, the image centroid position is the same as the intrinsic (unlensed) source position. At which time (and the corresponding source position) does the image centroid position agree with the source position? For a Schwarzschild lens, the image centroid position agrees with the source position only at $t = \pm\infty$, namely, $\beta = \infty$. To study this coincidence time (and source position), it is convenient to use Fig. 4 for $\hat{\theta}_{\rm pc}$ and $\hat{\beta}$ and Fig. 5 for $\delta\hat{\theta}_{\rm pc}$ and $\hat{\beta}$. Roughly speaking, the coincidence occurs at $\hat{\beta} \sim 1$–3, namely, a few times the Einstein crossing time. This time scale might be used for applications to observations.

C. Numerical computations: $\varepsilon < 0$ case

Next, we consider the $\varepsilon < 0$ case. Figure 6 shows the image centroid motion by the $\varepsilon < 0$ models. Note that the centroid curve does not exist for small $\hat{\beta}$ because of no images. See also Fig. 1 for no-image cases. Such a peculiar event might be misinterpreted as an eclipse in astronomy.

Figure 7 shows the image centroid shift by the $\varepsilon < 0$ models. There does not appear any bow-tie shape. Note that the image centroid shift is always negative because the effective force is repulsive. For unseen lens objects, the negative shift can be hardly distinguished from the positive one.

The centroid shift trajectory for the repulsive models might be elongated vertically to the source motion direction like a prolate spheroid as shown by Fig. 7, whereas that for convex-type attractive models such as the Schwarzschild one is tangentially elongated like an oblate spheroid (see Fig. 3). Figures 3 and 7 show that the size of the centroid shift by the repulsive models for each n and $\hat{\beta}_0$ is comparable to that for the corresponding $\varepsilon > 0$ models.

D. Parameter estimations

Equations (5) and (6) are rewritten as

$$\frac{|\bar{\varepsilon}|}{R_E^n} = \frac{D_S R_E}{D_{LS} D_L} = \frac{D_S \theta_E}{D_{LS}}. \tag{16}$$

Here, D_L, D_S, D_{LS}, and $R_E = D_L \theta_E$ are observables in astronomy, while $\bar{\varepsilon}$ and n are not direct observables but model parameters. Note that $\bar{\varepsilon}/R_E^n$ is comparable to the typical size of the deflection angle.

The right-hand side of Eq. (16) consists of the observables, and it is a dimensionless quantity. Hence, Eq. (16) allows us to investigate $|\bar{\varepsilon}|/R_E^n$ from observations. See Tables II and III for the Einstein ring size and Einstein radius crossing time, respectively. Near-future astrometry space missions such as Gaia and JASMINE are expected to have angular sensitivity of a few microarcseconds, for which the relevant parameter combination is limited as

TABLE II. Einstein radii and model parameters for Bulge and LMC lensings. θ_E is the angular Einstein radius, R_E is the Einstein radius, and $\bar{\varepsilon}$ and n are the two model parameters. $D_S =$ 8 kpc and $D_L = 4$ kpc are assumed for Bulge. $D_S = 50$ kpc and $D_L = 25$ kpc are assumed for LMC.

	Bulge		LMC	
θ_E (mas)	R_E (km)	$\frac{\bar{\varepsilon}}{R_E^n}$	R_E (km)	$\frac{\bar{\varepsilon}}{R_E^n}$
10^{-3}	6.0×10^5	1.0×10^{-11}	3.7×10^6	1.0×10^{-11}
10^{-2}	6.0×10^6	1.0×10^{-10}	3.7×10^7	1.0×10^{-10}
10^{-1}	6.0×10^7	1.0×10^{-9}	3.7×10^8	1.0×10^{-9}
1	6.0×10^8	1.0×10^{-8}	3.7×10^9	1.0×10^{-8}
10	6.0×10^9	1.0×10^{-7}	3.7×10^{10}	1.0×10^{-7}
10^2	6.0×10^{10}	1.0×10^{-6}	3.7×10^{11}	1.0×10^{-6}
10^3	6.0×10^{11}	1.0×10^{-5}	3.7×10^{12}	1.0×10^{-5}

TABLE III. Einstein radius crossing times for Bulge and LMC lensings. t_E is the Einstein radius crossing time. $D_S = 8$ kpc and $D_L = 4$ kpc are assumed for Bulge. $D_S = 50$ kpc and $D_L = 25$ kpc are assumed for LMC. $v_T = 220$ km/s is assumed for Bulge and LMC. In this table, the Einstein radius is calculated by $R_E = v_T \times t_E$ from the definition of the Einstein radius crossing time. Here, the input is $t_E \sim 10^{-3}$–10^3(day), namely, 1(min)–3(yr).

t_E (day)	R_E (km)	$\frac{\bar{\varepsilon}}{R_E^n}$ [Bulge]	$\frac{\bar{\varepsilon}}{R_E^n}$ [LMC]
10^{-3}	1.9×10^4	3.1×10^{-13}	5.0×10^{-14}
10^{-2}	1.9×10^5	3.1×10^{-12}	5.0×10^{-13}
10^{-1}	1.9×10^6	3.1×10^{-11}	5.0×10^{-12}
1	1.9×10^7	3.1×10^{-10}	5.0×10^{-11}
10	1.9×10^8	3.1×10^{-9}	5.0×10^{-10}
10^2	1.9×10^9	3.1×10^{-8}	5.0×10^{-9}
10^3	1.9×10^{10}	3.1×10^{-7}	5.0×10^{-8}

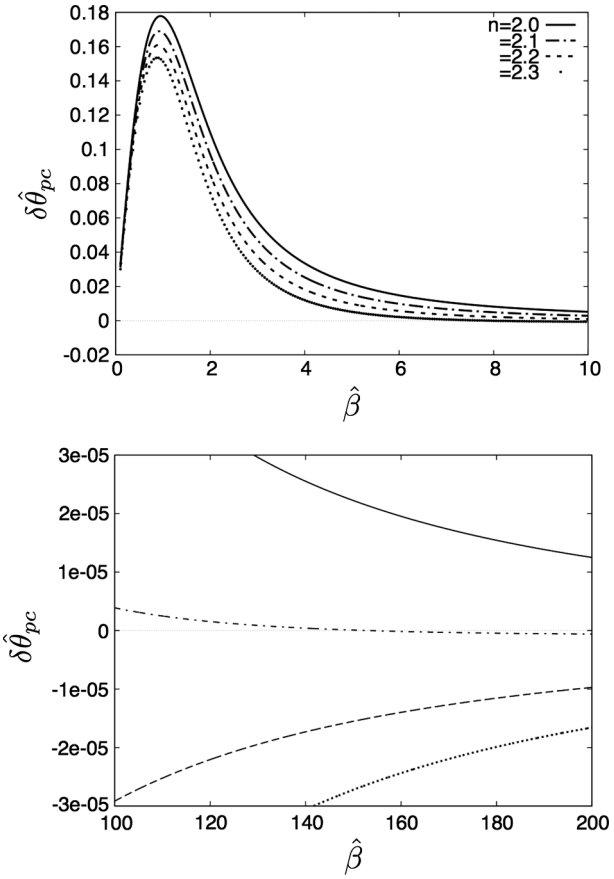

FIG. 8. Image centroid shift $\delta\hat{\theta}_{\rm pc}$ and $\hat{\beta}$ for $\varepsilon > 0$ (convex-type attractive models). The solid, dotted-dashed, dashed, and dotted curves denote $n = 2.0$, 2.1, 2.2, and 2.3, respectively. The horizontal axis denotes the source position $\hat{\beta}$ normalized by the Einstein radius, and the vertical axis denotes $\delta\hat{\theta}_{\rm pc}$. Top: $\hat{\beta} \in [0, 10]$. Bottom: $\hat{\beta} \in [100, 200]$.

$|\bar{\varepsilon}|/R_E^n > 10^{-11}$. Roughly speaking, the mission lifetime is several years, for which the relevant time scale is limited as $t_E <$ a few years, and Table III thus tells the limit as $|\bar{\varepsilon}|/R_E^n < 10^{-7}$ (for Bulge) and $< 10^{-8}$ [for Large Magellanic Cloud (LMC)]. In total, the parameter range relevant for the near-future missions is $10^{-11} < |\bar{\varepsilon}|/R_E^n < 10^{-7}$.

Before closing this section, we mention how large n models could lead to a multiply connected curve of the microlensed centroid shift. Numerical calculations suggest that $n > 2$ and $\varepsilon > 0$ models could produce a bow-tie shape. See also Fig. 8 for numerical computations in the vicinity of $n = 2$ as $n = 2.0$, 2.1, 2.2, and 2.3. The numerical calculations suggest that the bow-tie shape could appear if $n > 2$. Numerical computations for other parameter values suggest that the maximum numbers of the loops and the knots in the centroid curve are 3 and 1, respectively, which are actually achieved by the $n = 3$ model.

IV. DISCUSSION AND CONCLUSION

We examined gravitational lens models inspired by modified gravity theories, exotic matter, and energy. By using an asymptotically flat, static, and spherically symmetric spacetime model of which metric depends on the inverse distance to the power of positive n, it was shown in the weak-field and thin-lens approximations that, for large n cases in the convex-type models, the centroid shift from the source position might move on a multiply connected curve like a bow tie, while it is known to move on an ellipse for the $n = 1$ case and to move on an oval curve for $n = 2$. This bow-tie shape by the convex-type exotic lens models is distinguishable from standard ones due to binary motions or due the microlensing by a Schwarzschild lens. The distinctive feature such as the bow-tie shape may be used for searching (or constraining) localized exotic matter or energy with astrometric observations.

The parameter range relevant for the current and near-future missions such as Gaia and JASMIME is $10^{-11} < |\bar{\varepsilon}|/R_E^n < 10^{-7}$, where we assume that the accuracy in astrometry will reach a few microarcseconds and the mission lifetime will be several years.

It was shown also that the centroid shift trajectory for concave-type repulsive models might be elongated vertically to the source motion direction like a prolate spheroid, whereas that for convex-type attractive models such as the Schwarzschild one is tangentially elongated like an oblate spheroid. The image centroid shift by the repulsive models is always negative because the effective force is repulsive. For unseen lens objects, the negative shift can be hardly distinguished from the positive one. In this sense, it might be relatively difficult to investigate the repulsive models in astrometry.

ACKNOWLEDGMENTS

We would like to thank F. Abe, M. Bartelmann, T. Harada, S. Hayward, J. Kunz, K. Nakao, Y. Sendouda, R. Takahashi, N. Tsukamoto, and M. Visser for the useful conversations on the exotic lens models.

[1] S. Frittelli, T. P. Kling, and E. T. Newman, Phys. Rev. D **61**, 064021 (2000).
[2] K. S. Virbhadra and G. F. R. Ellis, Phys. Rev. D **62**, 084003 (2000).
[3] K. S. Virbhadra, Phys. Rev. D **79**, 083004 (2009).
[4] K. S. Virbhadra, D. Narasimha, and S. M. Chitre, Astron. Astrophys. **337**, 1 (1998).
[5] K. S. Virbhadra and G. F. R. Ellis, Phys. Rev. D **65**, 103004 (2002).
[6] K. S. Virbhadra and C. R. Keeton, Phys. Rev. D **77**, 124014 (2008).
[7] J. P. DeAndrea and K. M. Alexander, arXiv:1402.5630.
[8] E. F. Eiroa, G. E. Romero, and D. F. Torres, Phys. Rev. D **66**, 024010 (2002).
[9] V. Perlick, Phys. Rev. D **69**, 064017 (2004).
[10] H. G. Ellis, J. Math. Phys. (N.Y.) **14**, 104 (1973).
[11] M. S. Morris and K. S. Thorne, Am. J. Phys. **56**, 395 (1988).
[12] M. S. Morris, K. S. Thorne, and U. Yurtsever, Phys. Rev. Lett. **61**, 1446 (1988).
[13] M. Visser, *Lorentzian Wormholes: From Einstein to Hawking* (American Institute of Physics, New York, 1995).
[14] L. Chetouani and G. Clément, Gen. Relativ. Gravit. **16**, 111 (1984).
[15] G. Clément, Int. J. Theor. Phys. **23**, 335 (1984).
[16] M. Safonova, D. F. Torres, and G. E. Romero, Phys. Rev. D **65**, 023001 (2001).
[17] A. A. Shatskii, Astronomy Reports **48**, 525 (2004).
[18] K. K. Nandi, Y. Z. Zhang, and A. V. Zakharov, Phys. Rev. D **74**, 024020 (2006).
[19] F. Abe, Astrophys. J. **725**, 787 (2010).
[20] Y. Toki, T. Kitamura, H. Asada, and F. Abe, Astrophys. J. **740**, 121 (2011).
[21] N. Tsukamoto, T. Harada, and K. Yajima, Phys. Rev. D **86**, 104062 (2012).
[22] N. Tsukamoto and T. Harada, Phys. Rev. D **87**, 024024 (2013).
[23] C. M. Yoo, T. Harada, and N. Tsukamoto, Phys. Rev. D **87**, 084045 (2013).
[24] T. K. Dey and S. Sen, Mod. Phys. Lett. A **23**, 953 (2008).

[25] A. Bhattacharya and A. A. Potapov, Mod. Phys. Lett. A **25**, 2399 (2010).
[26] K. Nakajima and H. Asada, Phys. Rev. D **85**, 107501 (2012).
[27] G. W. Gibbons and M. Vyska, Classical Quantum Gravity **29**, 065016 (2012).
[28] S. Capozziello, V. F. Cardone, and A. Troisi, Phys. Rev. D **73**, 104019 (2006).
[29] Z. Horvath, L. A. Gergely, D. Hobill, S. Capozziello, and M. De Laurentis, Phys. Rev. D **88**, 063009 (2013).
[30] S. Mendoza, T. Bernal, X. Hernandez, J. C. Hidalgo, and L. A. Torres, Mon. Not. R. Astron. Soc. **433**, 1802 (2013).
[31] H. Asada, Prog. Theor. Phys. **125**, 403 (2011).
[32] Z. Horvath, L. Gergely, and D. Hobill, Classical Quantum Gravity **27**, 235006 (2010).
[33] N. Dadhich, R. Maartens, P. Papadopoulos, and V. Rezania, Phys. Lett. B **487**, 1 (2000).
[34] T. Kitamura, K. Nakajima, and H. Asada, Phys. Rev. D **87**, 027501 (2013).
[35] R. Takahashi and H. Asada, Astrophys. J. **768**, L16 (2013).
[36] H. Bondi, Rev. Mod. Phys. **29**, 423 (1957).
[37] M. Jammer, *Concepts of Mass in Classical and Modern Physics* (Harvard University, Cambridge, MA, 1961).
[38] M. Jammer, *Concepts of Mass in Contemporary Physics and Philosophy* (Princeton University, Princeton, NJ, 1999)
[39] J. G. Cramer, R. L. Forward, M. S. Morris, M. Visser, G. Benford, and G. A. Landis, Phys. Rev. D **51**, 3117 (1995).
[40] T. Piran, Gen. Relativ. Gravit. **29**, 1363 (1997).
[41] G. Gibbons and H. Kodama, Prog. Theor. Phys. **121**, 1361 (2009).
[42] K. Izumi, C. Hagiwara, K. Nakajima, T. Kitamura, and H. Asada, Phys. Rev. D **88**, 024049 (2013).
[43] M. A. Walker, Astrophys. J. **453**, 37 (1995).
[44] M. Miyamoto and Y. Yoshii, Astron. J. **110**, 1427 (1995).
[45] M. Hosokawa, K. Ohnishi, and T. Fukushima, Astron. J. **114**, 1508 (1997).
[46] N. Safizadeh, N. Dalal, and K. Griest, Astrophys. J. **522**, 512 (1999).
[47] Y. Jeong, C. Han, and S. Park, Astrophys. J. **511**, 569 (1999).
[48] G. F. Lewis and X. R. Wang, Prog. Theor. Phys. **105**, 893 (2001).
[49] H. Asada, Astrophys. J. **573**, 825 (2002).
[50] C. Han and C. Lee, Mon. Not. R. Astron. Soc. **329**, 163 (2002).
[51] Here, we mention the truncated expression in Eq. (1). Let us begin with considering a sphere for which the radius from the center is denoted as r. The mass inside the sphere is denoted as $M(r)$. Any physically reasonable theory of gravity must admit the Newtonian limit, in accordance with experiments and observations. Hence, the metric components g_{tt} and g_{rr} in the weak-field region are expected to have the Newton-type potential written as $M(r)/r$. Note that the part of $1/r$ comes from the Green function for the Laplacian operator (and thus the Poisson equation). The fraction as $M(r)/r$ becomes the inverse distance only for a point mass case, while it is a more general function of the distance for extended objects. Roughly speaking, therefore, the ansatz of the spacetime metric, Eq. (1), might correspond to assuming $M(r)$ in the power law of r. For example, $n = 0$, $n = 1$, and $n = 2$ correspond to isothermal spheres (as a simple model of a galaxy), the vacuum region outside of a bounded mass distribution, and Ellis wormholes, respectively. Ellis wormholes are nonvacuum and nonsingular (regular) in the sense that they are associated with a particular scalar field configuration. Models under study thus describe a regular distribution of matter for $n \neq 1$.
[52] P. Schneider, J. Ehlers, and E. E. Falco, *Gravitational Lenses* (Springer, New York, 1992).
[53] C. Claudel, K. S. Virbhadra, and G. F. R. Ellis, J. Math. Phys. **42**, 818 (2001).